Mesoscale modeling of photoelectrochemical devices: light absorption and carrier collection in monolithic, tandem, Si|WO_3 microwires

Katherine T. Fountaine[1,2] and Harry A. Atwater[2,3,*]

[1]*Department of Chemistry and Chemical Engineering, California Institute of Technology, 1200 E. California Blvd., Pasadena, California 91125, USA*
[2]*Joint Center for Artificial Photosynthesis, 1200 E. California Blvd., Pasadena, California 91125, USA*
[3]*Department of Applied Physics and Materials Science, California Institute of Technology, 1200 E. California Blvd., Pasadena, California 91125, USA*
[*]*kfountai@caltech.edu*

Abstract: We analyze mesoscale light absorption and carrier collection in a tandem junction photoelectrochemical device using electromagnetic simulations. The tandem device consists of silicon ($E_{g,Si}$ = 1.1 eV) and tungsten oxide ($E_{g,WO3}$ = 2.6 eV) as photocathode and photoanode materials, respectively. Specifically, we investigated Si microwires with lengths of 100 μm, and diameters of 2 μm, with a 7 μm pitch, covered vertically with 50 μm of WO_3 with a thickness of 1 μm. Many geometrical variants of this prototypical tandem device were explored. For conditions of illumination with the AM 1.5G spectra, the nominal design resulted in a short circuit current density, J_{SC}, of 1 mA/cm^2, which is limited by the WO_3 absorption. Geometrical optimization of photoanode and photocathode shape and contact material selection, enabled a three-fold increase in short circuit current density relative to the initial design via enhanced WO_3 light absorption. These findings validate the usefulness of a mesoscale analysis for ascertaining optimum optoelectronic performance in photoelectrochemical devices.

OCIS codes: (220.0220) Optical design and fabrication; (220.2740) Geometric optical design; (230.0250) Optoelectronics; (040.5350) Photovoltaic; (160.6000) Semiconductor materials.

References and links

1. A. Bard and M. A. Fox, "Artificial photosynthesis: solar splitting of water to hydrogen and oxygen," Acc. Chem. Res. **28**(3), 141–145 (1995).
2. F. E. Osterloh and B. A. Parkinson, "Recent developments in solar water-splitting photocatalysis," MRS Bull. **36**(1), 17–22 (2011).
3. B. Masters, "Three-dimensional microscopic tomographic imagings of the cataract in a human lens in vivo," Opt. Express **3**(9), 332–338 (1998).
4. A. J. Nozik, "Photoelectrochemical cells," Philos. Trans. R. Soc. Lond. A **295**(1414), 453–470 (1980).
5. D. G. Nocera, "The artificial leaf," Acc. Chem. Res. **45**(5), 767–776 (2012).
6. S. Haussener, C. Xiang, J. M. Spurgeon, S. Ardo, N. S. Lewis, and A. Z. Weber, "Modeling, simulation, and design criteria for photoelectrochemical water-splitting systems," Energy Environ. Sci. **5**(12), 9922–9935 (2012).

M. R. Shaner, K. T. Fountaine, S. Ardo, R. H. Coridan, H. A. Atwater, and N. S. Lewis, "Photoelectrochemistry of core-shell tandem junction n-p+ -Si/n-WO_3 microwire array photoelectrodes," Energy Environ. Sci. **7**(2), 779–790 (2014).

8. B. M. Kayes, M. A. Filler, M. C. Putnam, M. D. Kelzenberg, N. S. Lewis, and H. A. Atwater, "Growth of vertically aligned Si wire arrays over large areas (>1 cm^2) with Au and Cu catalysts," Appl. Phys. Lett. **91**(10), 103110 (2007).
9. J. R. Bolton, S. J. Strickler, and J. S. Connolly, "Limiting and realizable efficiencies of solar photolysis of water," Nature **316**(6028), 495–500 (1985).
10. R. E. Rocheleau and E. L. Miller, "Photoelectrochemical production of hydrogen: engineering loss analysis," Int. J. Hydrogen Energy **22**(8), 771–782 (1997).
11. B. M. Kayes, H. A. Atwater, and N. S. Lewis, "Comparison of the device physics principles of planar and radial p-n junction nanorod solar cells," J. Appl. Phys. **97**(11), 114302 (2005).

#217642 - $15.00 USD Received 23 Jul 2014; accepted 23 Aug 2014; published 5 Sep 2014

12. E. Ertekin, P. A. Greaney, D. C. Chrzan, and T. D. Sands, "Equilibrium limits of coherency in strained nanowire heterostructures," J. Appl. Phys. **97**(11), 114325 (2005).
13. N. C. Strandwitz, D. B. Turner-Evans, A. C. Tamboli, C. T. Chen, H. A. Atwater, and N. S. Lewis, "Photoelectrochemical behavior of planar and microwire array Si|GaP electrodes," Adv. Energy Mater. **2**(9), 1109–1116 (2012).
14. S. Trasatti, "Work function, electronegativity, and electrochemical behavior of metals: III. Electrolytic hydrogen evolution in acid solutions," J. Electroanal. Chem. Interfacial Electrochem. **39**(1), 163–184 (1972).
15. A. Subrahmanyam and A. Karuppasamy, "Optical and electrochromic properties of oxygen sputtered tungsten oxide (WO3) thin films," Sol. Energy Mater. Sol. Cells **91**(4), 266–274 (2007).
16. K. Sugiyama, H. Ishii, Y. Ouchi, and K. Seki, "Dependence of indium-tin-oxide work function on surface cleaning method as studied by ultraviolet and x-ray photoemission spectroscopies," J. Appl. Phys. **87**(1), 295–298 (2000).
17. M. D. Kelzenberg, Silicon Microwire Photovoltaics, (California Institute of Technology, 2010).
18. E. L. Warren, S. W. Boettcher, M. G. Walter, H. A. Atwater, and N. S. Lewis, "pH-independent, 520mV open-circuit voltages of Si/methyl viologen(2+/+) contacts through use of radial n(+)p-Si junction microwire array photoelectrodes," J. Phys. Chem. C **115**(2), 594–598 (2011).
19. T. Iwai, "Temperature dependence of the optical absorption edge of tungsten trioxide single crystal," J. Phys. Soc. Jpn. **15**(9), 1596–1600 (1960).
20. W. A. Gerrard, "Photoelectrolysis using a tungsten-oxide anode in chlorine and sulfate-solutions," J. Electroanal. Chem. **86**(2), 421–424 (1978).
21. Q. Mi, A. Zhanaidarova, B. S. Brunschwig, H. B. Gray, and N. S. Lewis, "A quantitative assessment of the competition between wafer and anion oxidation at WO3 photoanodes in acidic aqueous electrolytes," Energy Environ. Sci. **5**(2), 5694–5700 (2012).
22. A. Leenheer, Light to electrons to bonds: imaging water splitting and collecting photoexcited carriers (California Institute of Technology, 2013).
23. K. R. Reyes-Gil, B. S. Brunschwig, and N. S. Lewis, "Enhanced photogenerated carrier diffusion and quantum yields in highly ordered porous WO_3 photoanodes for solar water oxidation," unpublished manuscript, 1–35.
24. J. M. Berak and M. Sienko, "Effect of oxygen-deficiency on electrical transport properties of tungsten trioxide crystals," J. Solid State Chem. **2**(1), 109–133 (1970).
25. H. Raether, *Surface Plasmons* (Springer, 1988).
26. C. Kittel, *Introduction to Solid State Physics*, 7th ed. (Wiley, 1996).

1. Introduction

For solar power to be feasible at the terawatt scale, a method to store and dispatch solar energy must be developed. Solar-generated chemical fuels have potential for large-scale storage and distribution, and most routes to solar fuels begin with hydrogen formed via photoelectrolysis of water [1–3]. Currently, commercially available technologies carry out solar fuel generation in two steps: (1) solar to electric conversion using photovoltaics, and (2) water electrolysis to form hydrogen using an electrolyzer. Combining these two steps into one photoelectrochemical device can potentially reduce material usage and cost and increase efficiency by combining the photogeneration and electrochemical energy conversion steps [4].

The design and fabrication of an efficient and inexpensive photoelectrochemical (PEC) device is a complex task, with many issues that need to be addressed, extending from the molecular level all the way up to the module level [5,6].This paper focuses on the mesoscale (10s of nm to ~100s of μm), where light absorption, charge carrier transport, catalysis, and transport of reactants and products through multiphase solutions and ion-conducting membranes are inherently integrated. Figure 1 illustrates this concept for the case of a schematic tandem photoelectrochemical device with one-dimensional transport pathways. Realistic two- and three-dimensional nano- and microstructures have somewhat different detailed absorption and transport characteristics but function in a broadly similar fashion. Material selection, electrolyte solution properties and geometric device design are coupled to these transport phenomena and greatly affect device performance. Understanding and optimizing device operation on the mesoscale is crucial to achieve high efficiency photoelectrochemical device performance. Because light absorption, electronic transport, interfacial redox reactions and ionic transport are coupled in photoelectrolysis, a solely empirically-based iterative device design approach is impractical and time-intensive. A simulation-driven design approach enables us to quickly identify and understand the limiting factors in photoelectrochemical device operation and use this knowledge to optimize device performance.

#217642 - $15.00 USD Received 23 Jul 2014; accepted 23 Aug 2014; published 5 Sep 2014

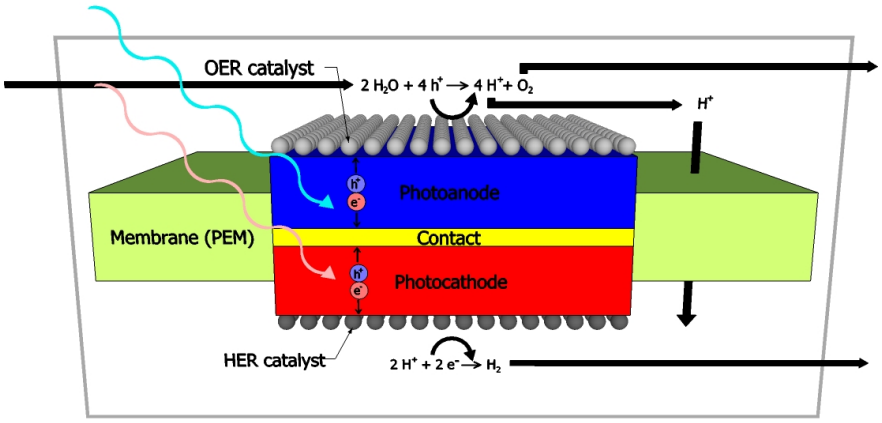

Fig. 1. One-dimensional representation of a tandem photoelectrochemical device with a proton-conducting membrane, illustrating the integrated nature of light absorption, carrier transport, catalysis, and reactant and product transport through solution and membrane.

Our report here focuses on optoelectronic effects manifest at the mesoscale, demonstrating how geometric design parameters and optical materials selection can greatly alter the absorption efficiency for a photoelectrochemical device for given photoabsorber materials. Specifically, we demonstrate that modest geometrical modifications to a microwire photoelectrochemical device design can result in a three-fold increase in light absorption and short circuit current relative to a nominal baseline design.

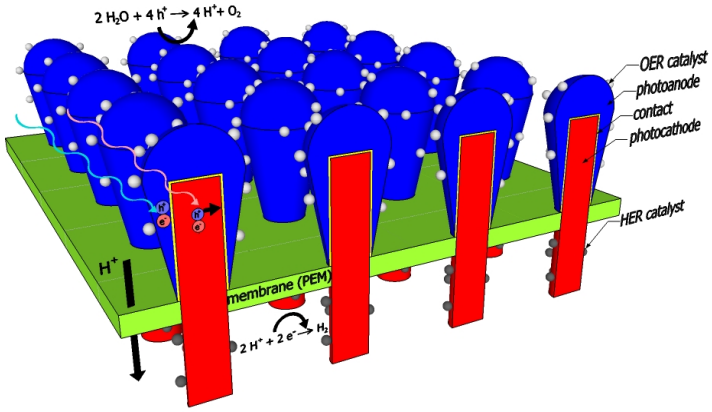

Fig. 2. Diagram of a monolithic, tandem, microwire based PEC device, including photoanode, photocathode, Ohmic contact material between the two photoelectrodes, oxygen (OER) and hydrogen (HER) evolution catalysts, and ion-conducting membrane. Reactions are written for acidic conditions, and therefore, the membrane is labeled as a proton exchange membrane (PEM).

We explore design aspects for a tandem, monolithic, microwire-based silicon (Si) | tungsten oxide (WO_3) photoelectrochemical device [Fig. 2]. Experimental fabrication of one variant of this design has been demonstrated [7]. This design was inspired by the recent development of Si microwire synthesis processes for photovoltaic applications [8]. Deposition of a series-connected photoanode material on Si microwires enables a tandem device to be realized, with an open circuit voltage suitable for water splitting, and enables greater use of the solar spectrum in a tandem photoabsorber [9,10]. This tandem, microwire design affords many advantages including (i) the series addition of the photovoltages in both components of the tandem to exceed the minimum voltage required to split water, while simultaneously absorbing visible light [8], (ii) the orthogonalization of light absorption (in

#217642 - $15.00 USD Received 23 Jul 2014; accepted 23 Aug 2014; published 5 Sep 2014

wire axial direction) and carrier transport (in wire radial direction), which is especially advantageous for indirect bandgap semiconductors, which have long absorption lengths [11], (iii) increased surface area for catalysis, (iv) an approximately 90% decrease in photoelectrode material usage relative to planar monolithic device designs, depending on wire pitch and diameter, (v) a source for radial strain relief, enabling the integration of lattice mismatched materials [12,13], (vi) a monolithic structure enabling straightforward incorporation of an ion-conducting membrane, and (vii) short electrolyte diffusion pathways for low solution resistance [6].

We explored two optoelectronic variations of microwire tandem absorbers (illustrated in Fig. 3) and investigated design features that increase light absorption without compromising carrier collection. The main difference between the two variations is the optical opacity or transparency of the contact material interconnecting the two photoelectrodes. An opaque contact design increases the photon path length, and thus absorption, in the photoanode, which is crucial for wide bandgap materials, while the transparent contact design reduces absorption losses in the contact layer. Opaque aluminum (Al) and transparent indium tin oxide (ITO) contacts were investigated because their electron affinities facilitate formation of an ohmic contact to WO_3 [14–17]. The optical characteristics of these contact materials and of the Si photocathode and WO_3 photoanode motivated the different doping schemes shown. Si is an attractive choice for the photocathode material owing to the existing knowledge base for design and fabrication of Si microwire arrays with good fidelity and electronic quality [8,17]. A buried p|n Si junction enables a larger open circuit voltage (V_{OC}) and more ideal behavior than the feasible alternative, i.e., a liquid junction between p-Si and the H^+/H_2 redox couple [18]. In both optoelectronic designs, the solution interface consists of degenerately doped n-Si to facilitate tunneling for nearly lossless charge transfer. Similarly, the contact interface with degenerately doped p-Si creates a tunneling ohmic contact. However it is desirable to locate the p|n junction in close proximity to the areas of greatest light absorption, viz. the bottom half of the wire in the opaque contact design and the top half of the wire in the transparent contact design. Despite its wide optical bandgap (E_g = 2.6eV) [19], WO_3 is an appropiate photoanode material because it is stable under oxidizing and acidic conditions [20], and is intrinsically n-type, enabling facile creation of a liquid junction with the H_2O/O_2 redox couple [21]. These properties enable experimental fabrication, and thus, comparison of experiment and theory for this design [7].

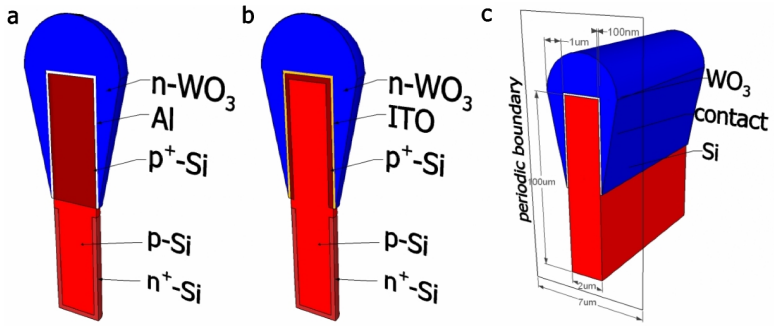

Fig. 3. Schematics for two proposed optoelectronic tandem PEC designs; (a) an opaque contact with the p|n junction in the bottom half of the Si microwire (b) a transparent contact design with the p|n junction in the top half of the Si microwire.

2. Design approach

The complex dielectric function (*n*, *k*) data for each material and the tandem microwire geometric configuration (Fig. 4(a)) were used to render microstructures simulated by finite

#217642 - $15.00 USD Received 23 Jul 2014; accepted 23 Aug 2014; published 5 Sep 2014

difference time domain method numerical solutions to Maxwell's equations using Lumerical FDTD. The nominal design dimensions are defined by 7 μm period square microwire arrays consisting of 100 μm tall silicon microwires with 1 μm radii; the top 50 μm of the wires are conformally coated with 100 nm of either Al or ITO contact material and 1 μm of WO_3. The nominal photoanode geometry mimicked the shape of experimental WO_3 photoanodes (Fig. 3). Periodic arrays of the structure in the y-direction were defined via periodic Bloch boundary conditions. Perfectly-matched layer (PML) boundaries were used at the top and bottom of the simulation region to create boundaries with nearly 100% transmission. The bottom boundary was chosen to be metallic for designs incorporating a back reflector. The void space between microstructures was modeled as air in the results presented below, but insignificant changes in absorbed current (~1-2%) were observed when the structures were immersed in water, which does not absorb significantly in the UV-Vis range.

Full field (*E*, *H*) electromagnetic simulations performed in two dimensions were used to investigate light propagation and absorption in these microstructures at discrete wavelengths, ranging from 350 to 1100 nm in 50 nm intervals [17]. Transverse electric (TE) polarization, defined as an electric field oscillating in the *xy* plane, was used to illuminate the structures. Partial spectral averaging was employed in all simulations to eliminate large fluctuations in reflection and transmission that occur at specific wavelengths in thin substrates due to interference phenomena such as Newton's rings [17]. By recording the spatially-resolved electric field, the normalized power absorption (P_{abs}) in each material was calculated using Eq. (1), where E is the electric field, ϵ is the material permittivity, and ω is angular frequency [17].

$$P_{abs} = -\frac{1}{2}\omega|E|^2 \, imag(\varepsilon) \tag{1}$$

By spatially integrating this expression, the fraction of power absorbed in each material at a given wavelength was calculated. From these absorption calculations, the device's ideal short circuit current density (IQE = 1) was calculated using the AM1.5G Spectrum. Performing this procedure at multiple angles of incidence (0 to 60°) and weighting appropriately allowed the calculation of the ideal day-integrated hydrogen production based on the current-limiting photoelectrode performance and the assumption of unity Faradaic efficiency. Ideal short circuit current density at normal incidence and day-integrated hydrogen production per unit area are used as figures of merit for the designs considered.

Carrier transport simulations were performed using Synopsys TCAD Sentaurus, which solves in a coupled fashion the Poisson equation and charge carrier transport equations for charge carriers using a finite element (FE) method. Device microstructures were rendered to precisely match the discretization used in the full-field electromagnetic simulations in two dimensions using radial symmetry. To create a coupled optoelectronic simulation, spatially resolved carrier generation rates for normal incidence illumination were calculated from the electric field and complex index maps obtained from Lumerical FDTD results [Eq. (2)] and used as the optical inputs for carrier transport simulations in Sentaurus.

$$C_{gen} = \frac{\pi|E|^2 \, imag(\varepsilon)}{h} \tag{2}$$

Charge carrier transport simulations were performed only for the WO_3|liquid junction because it limits device performance. The diffusion length of 1 μm with Shockley-Read-Hall recombination and a donor doping concentration of 10^{15} cm^{-3} were used for WO_3. The development of the WO_3 material parameter file is detailed in a previous publication [6]. The WO_3|liquid junction was modeled as a Schottky junction, using thermionic emission physics, with the contact work function equaling that of the oxygen evolution reaction redox potential under standard conditions (5.68 eV relative to vacuum). Short circuit current densities for each structure were determined by solving the coupled Poisson and charge carrier equations

#217642 - $15.00 USD Received 23 Jul 2014; accepted 23 Aug 2014; published 5 Sep 2014

under illumination and no applied bias. Bulk and surface recombination currents were extracted from the software, as well.

3. Results and discussion

3.1 Original designs

Plots of normal incidence absorption vs. wavelength for Si, WO_3, and the contact material in the two original designs [Fig. 3] are shown in Figs. 4(b) and 4(c) and compared to a planar device with thickness giving equal material volume (w_{Si} = 6.4 μm, w_{WO3} = 5 μm, w_{ITO} = 0.7 μm). ITO was used as the contact material in these planar comparisons because aluminum (w = 0.7 μm) would block all light from the silicon. Table 1 displays the normal incidence ideal short circuit current densities, ideal day-integrated hydrogen production density, normal incidence internal quantum efficiencies, normal incidence short circuit current densities, and current density losses due to bulk and surface recombination for each design and its planar equivalent.

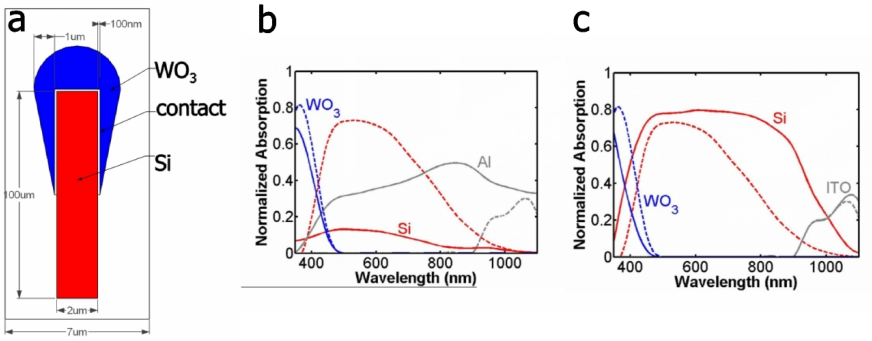

Fig. 4. (a) Schematic of simulation unit cell, simulated as a 2D infinite array using TE-polarized illumination at normal incidence; (b) absorption vs. wavelength for the photoanode (WO_3), photocathode (Si), and contact (Al, opaque) for the structure in (a); (c) absorption vs. wavelength for the photoanode (WO_3), photocathode (Si), and contact (ITO, transparent) for the structure in (a).

Table 1. Short Circuit Current Densities (mA/cm^2), Day-integrated Hydrogen Production (mmol day^{-1}cm^{-2}), and Internal Quantum Efficiencies for the Opaque and Transparent Contact Designs and Their Planar Equivalence

Model	j_{Si}	j_{WO3}	$j_{Contact}$	j_{Ref}	j_{Trans}	F_{H2}	IQE	j_{SC}	j_{BR}	j_{SR}
Opaque	3.21	1.46	16.72	18.07	5.52	0.09	0.86	1.26	0.03	0.17
Transparent	28.31	1.02	2.11	5.69	7.86	0.17	0.88	0.90	0.02	0.20
Planar	16.53	1.75	0.20	16.19	8.86	0.26	0.57	1.00	0.54	0.21

The significantly lower absorbed current density of WO_3 in comparison to Si in all designs illustrates that WO_3, due to its wide bandgap, absorbs far less light than Si and limits device current and hydrogen production in both cases. Because of aluminum's reflective properties, the opaque contact design outperforms the transparent contact design at normal incidence due to an increased photon path length and, hence, greater absorption in WO_3. However, the transparent contact design outperforms the opaque contact design in day-integrated hydrogen production because aluminum absorption in the opaque contact design increases and transmission in the transparent contact design decreases with increasing incidence angle. Absorption in the WO_3 is limited by contact absorption in the opaque contact design and silicon absorption in the transparent contact design, which has significant ramifications for light absorption optimization and is discussed later in this text.

Neither of the microstructured designs outperforms the equivalent planar device optically, mainly due to a longer, uninterrupted photon path length through the WO_3 in the planar case. However, when complete optoelectronic performance is taken into account, the transparent

#217642 - $15.00 USD Received 23 Jul 2014; accepted 23 Aug 2014; published 5 Sep 2014

model approaches and the opaque contact model outperforms the planar equivalent device. Both of the microstructured devices have higher internal quantum efficiencies than the planar device because they have shorter carrier diffusion pathways thereby minimizing bulk recombination. In fact, the dominant loss in the microstructured designs is surface recombination at the Ohmic contact rather than the bulk recombination which dominates losses in the planar case. The higher internal quantum efficiencies of the two microstructured devices underscores the advantage of orthogonalizing the directions of light absorption and carrier collection for materials like WO_3 (reported L_D = 200nm-1um) [22–24] that have indirect optical bandgaps and relatively low material quality.

3.2 Loss in surface plasmon polariton modes

In the opaque contact design, significant absorption losses result from contact absorption (16.72 mA/cm^2), reflection (18.07 mA/cm^2) and transmission (5.52 mA/cm^2). While losses to reflection and transmission can be minimized with an appropriate antireflective (AR) coating, a back reflector, and smaller pitch size, the losses to contact absorption, 0.78 mA/cm^2 of which lie within the WO_3 band edge, present a more complex optimization problem. Experimental measurements of optically-thick planar aluminum indicate 93% reflection and 7% absorption; therefore, a simple ray optics framework cannot explain the absorption results for aluminum in the microwire structure. Observation of the electric field propagation in time revealed that light couples into a lossy surface plasmon-polariton (SPP) mode at the WO_3|Al interface. For ease of visual demonstration, Fig. 5 displays snapshots of the SPP mode propagating at 200 and 800 nm wavelengths along an Al|air interface, eliminating any convolution with the complex structure geometry and the absorption constant of WO_3. At λ = 800 nm [Fig. 5(a)], the evanescent decay of the electric field away from the interface, a signature of an SPP mode [25], is readily evident. At λ = 200 nm [Fig. 5(b)], as the wavelength of light approaches the Al|air SPP resonance of 113 nm [26], the decay length decreases and the speed of light that is trapped in the SPP mode slows notably in comparison to the plane wave, another signature of an SPP mode [25]. The surface wave disappeared at wavelengths shorter than the resonant wavelength. Similar observations were made for the WO_3|Al interface within the complete microstructure.

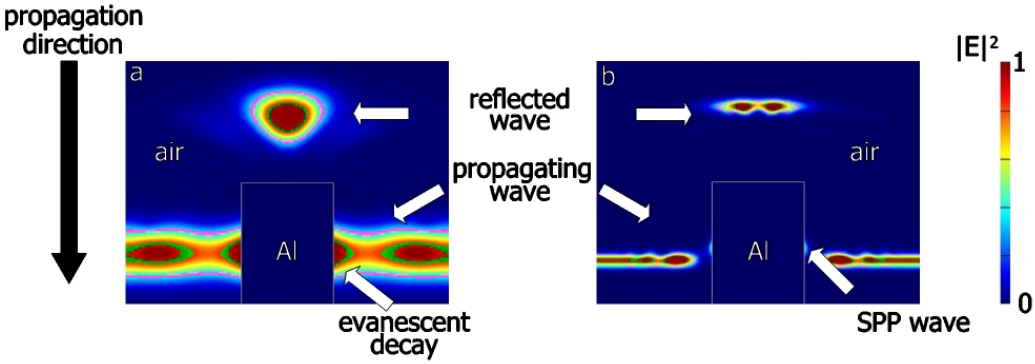

Fig. 5. Snapshots of the propagation of the electric field along an Al|air interface within an infinite 2D array of wires indicating the coupling into a surface plasmon-polariton mode (a) at λ = 800 nm, illustrating the evanescent decay of the electric field away from the interface; (b) at λ = 200 nm, illustrating the slower propagation of light at the interface.

Given that the lossy SPP mode at the WO_3|Al interface is the source of absorption in the aluminum, optimization of the opaque contact structure requires eliminating or, at a minimum, greatly reducing the amount of light that couples into this mode. A plethora of approaches were employed including reduction of aluminum, both in coverage area and thickness, alteration of the shape of the WO_3 and the Al, and replacement of Al with Ag (silver). A detailed discussion of results for these structures is beyond the scope of this paper,

#217642 - $15.00 USD Received 23 Jul 2014; accepted 23 Aug 2014; published 5 Sep 2014

but none of these approaches eliminated coupling into the SPP mode; this robust coupling capability of the microwire structure is attributed to the scattering properties of the wires. The most successful approach was the replacement of Al with Ag, resulting in a ~40% reduction in the contact absorption. Silver's red-shifted plasmon resonance and lower absorption coefficient throughout the visible in comparison to aluminum contribute to its lower absorption. Nevertheless, the 9.68 mA/cm^2 that is absorbed by Ag is large and places an inherent limit on the overall device performance. Despite the seemingly promising initial performance of the opaque contact design, these results motivate a more detailed analysis and optimization of the transparent contact design due to its greater potential for light absorption optimization.

3.3 Optimization

In the transparent contact design, the contact absorption is insignificant in the UV and visible region and minimal in the infrared region. Silicon absorbs over an order of magnitude more light than the WO_3; thus, the following optimization focuses solely on improving WO_3 optoelectronic performance, even at the expense of silicon absorption. As previously mentioned, the main sources of absorption loss for WO_3 within its band edge are from reflection, transmission and absorption in the silicon. Increasing the WO_3 thickness is the simplest approach to increase its absorption, but this method is constrained by the electronic performance of the material. Based on preliminary experimental measurements, the diffusion length of WO_3 is ~1 μm [22], which suggests that increasing the thickness of WO_3 beyond its current 1 μm thick coverage would have diminishing returns. Thus, other alterations to the original design were made iteratively in order to find an optimized structure for light absorption that should have comparable electrical performance with the original design. The most logical alterations include the reduction of the array pitch (7 μm to 5 μm for the optimized structure) to increase the amount of light that first interacts with the WO_3, the addition of an antireflective (AR) coating (100 nm of SiO_2 coating the upward-facing portion of the WO_3|air interface) to reduce reflection, and the addition of a back reflector (smooth metal surface) to eliminate transmission. Another alteration towards improving WO_3 absorption was the flattening of the top of the WO_3 in order to (i) reduce reflection at the WO_3|air interface and (ii) decrease silicon absorption within the WO_3 band edge by directing light downwards into the WO_3 as opposed to bending light towards the silicon wire. The shape of the top half of the silicon wire was etched into a cone shape in order to promote scattering back into the WO_3 at the ITO|WO_3 interface.

Schematics, absorption characteristics, and optoelectronic performance metrics for the original transparent model, a partially optimized structure, and the optimized structure along with their planar equivalent thickness structures are shown and compared in Fig. 6 and Table 2. The partially-optimized structure includes the conically-shaped silicon and an AR coating; its planar equivalent (w_{Si} = 4.3 μm, w_{WO3} = 7.6 μm, w_{ITO} = 0.2 μm) also includes an AR coating. The optimized structure includes all modifications discussed above; its planar equivalent (w_{Si} = 8.4 μm, w_{WO3} = 14.6 μm, w_{ITO} = 0.4 μm) includes an AR coating and back reflector. At normal incidence, the WO_3 in the optimized structure absorbs 230% more light and collects 240% more current than in the original transparent contact model and 130% more light and 140% more current than the opaque contact model. Despite an increase in bulk recombination due to the addition of oxide material per structure as well as per aerial area, the internal quantum efficiency of the optimized design is also slightly higher than that of the original because a smaller fraction of the minority carriers are recombining at the Ohmic contact. The absorption enhancements of the optimized design extend over all angles of incidence, resulting in a 140% increase in hydrogen production over the original transparent contact model and a striking 350% increase over the opaque contact model. Additionally, the optimized model outperforms its planar equivalent device in both optical and optoelectronic efficiency, highlighting the advantages of light guiding and scattering properties of the optimized microstructured devices.

#217642 - $15.00 USD Received 23 Jul 2014; accepted 23 Aug 2014; published 5 Sep 2014

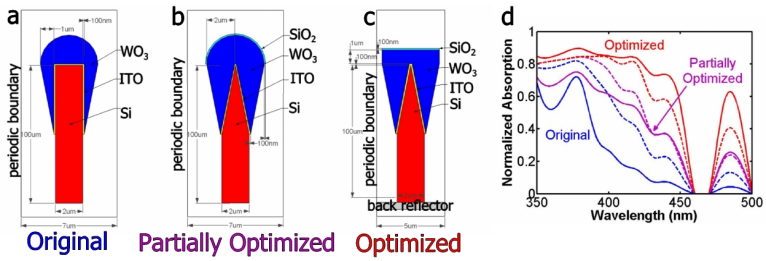

Fig. 6. Schematic of (a) the original, (b) the partially optimized, and (c) the optimized microwire array designs with the transparent, indium tin oxide contact; (d) plot of WO_3 absorption vs. wavelength of each structure and their planar equivalences, demonstrating the absorption enhancement.

Table 2. Short Circuit Current Densities (mA cm^{-2}), Day-integrated Hydrogen Production (mmol $day^{-1}cm^{-2}$), and Internal Quantum Efficiencies for the Original, Partially-optimized, and Optimized Transparent Contact Designs and Their Planar Equivalences

Model	j_{Si}	j_{WO3}	$j_{Contact}$	j_{Ref}	j_{Trans}	F_{H2}	IQE	j_{SC}	j_{BR}	j_{SR}
Original	28.31	1.02	2.11	5.69	7.86	0.17	0.88	0.90	0.02	0.20
Planar	16.53	1.75	0.20	16.19	8.86	0.26	0.57	1.00	0.54	0.21
Part. Opt.	28.10	2.10	5.12	1.04	8.70	0.34	0.85	1.79	0.11	0.20
Planar	14.79	2.03	0.58	16.57	9.59	–	0.49	1.00	0.88	0.15
Optimized	33.50	3.39	6.06	2.09	0.00	0.40	0.90	3.05	0.12	0.22
Planar	17.31	2.43	1.46	14.55	7.83	–	0.41	0.99	1.39	0.05

5. Conclusion

This coupled electromagnetic simulation/carrier transport investigation of the optoelectronic performance of tandem Si|WO_3 microwire arrays reveals that geometric design and the contact material selection can significantly influence light absorption properties. Furthermore, opaque contacts are not a realistic choice for the interface between the two semiconductors because they absorb a substantial amount of light, thereby reducing the overall device efficiency. Also, antireflective coatings, back reflectors and reduction of array period are powerful handles for increasing efficiency. We note that the Si|WO_3 system is not an ideal material combination for tandem devices due to the excessively wide bandgap of WO_3, but the optoelectronic results from this system are instructive for any system where the photoanode current density is limiting.

Additionally, this study reveals the value of full wave electromagnetic simulations coupled to charge carrier transport simulations for mesoscale design of photoelectrochemical devices. Simulation tools can quantitatively predict optoelectronic performance for realistic geometries and identify absorption-limiting phenomena, such as the lossy SPP mode in the opaque contact design, more quickly and efficiently than via a large number of experiments. These observations would be difficult, if not impossible, to make experimentally. Device models were developed and optoelectronic performance analyzed for roughly 50 design variations over the span of approximately six months, demonstrating the speed at which model-based device optimization can occur.

Acknowledgments

This material is based upon work performed by the Joint Center for Artificial Photosynthesis, a DOE Energy Innovation Hub, supported through the Office of Science of the U.S. Department of Energy under Award No. DE-SC0004993. K.T.F. is supported by the National Science Foundation Graduate Research Fellowship under Grant No. DGE-1144469. C.G.K. was supported by a Caltech Summer Undergraduate Research Fellowship.